3rd Trondheim Gas Technology Conference, TGTC-3

Modelling of heat transport in two-phase flow and of mass transfer between phases using the level-set method

M. Aa. Gjennestad[a,b,*], S. T. Munkejord[a]

[a]*SINTEF Energy Research, P.O. Box 4671 Sluppen, NO-7465 Trondheim, Norway*
[b]*Department of Physics, Norwegian University of Science and Technology, NO-7491 Trondheim, Norway*

Abstract

We describe mathematical models for heat transport and for mass transfer between phases due to vaporization and condensation. These models have been implemented in a framework for detailed two-phase flow calculations based on the level-set method. For two simple cases we show that simulated results agree with the corresponding analytical solutions and we demonstrate first-order convergence of the implemented methods. We also simulate a more physically realistic, three-dimensional case that is assumed rotationally symmetric around an axis. In this case, a droplet of liquid methane is vaporized and it is shown that the model yields results that are consistent with qualitative expectations.

1. Introduction

A large part of the greenhouse-gas emissions from production, transport and combustion of liquefied natural gas (LNG) is incurred during liquefaction [13]. Therefore there is a great potential for enabling a more energy-efficient and less emission-intense LNG life cycle by optimizing the liquefaction stage. Any reduction in energy consumption in the processing could also be beneficial from a financial point of view.

The design and operation of LNG plants is complex and requires experience data. This makes it challenging to account for new situations and perform optimizations. Even though some optimizations can be performed with more conventional engineering approaches, a better and more detailed understanding of the underlying physical behaviour of the fluid streams involved in the liquefaction is essential. According to Kunugi [6], there seems to be a general consensus in the scientific community that direct numerical simulation is one of the most promising approaches towards clarifying heat transfer characteristics and condensation/boiling phenomena and discussing their mechanisms.

In this work, models for heat transport and mass transfer between phases due to vaporization and condensation have been implemented in a framework for detailed two-phase flow calculations. This framework

---

*Corresponding author.
Email address: magnus.gjennestad@sintef.no (M. Aa. Gjennestad)

uses the level-set method to capture the interface, in combination with the ghost-fluid method (GFM) to treat interfacial discontinuities sharply and the continuum surface forces (CSF) method to treat the discontinuities in a diffuse manner. The aim was to enable detailed numerical studies of flow and heat transport in natural gas while accounting for vaporization and condensation.

The level-set method was first described by Osher and Sethian [10] and has since been used in two-phase flow models, both compressible and incompressible [9]. A review of some of the early advances in the use of this method to study boiling phenomena is given by Dhir [1]. In this work, however, we consider a more recent level-set-based model for vaporization and condensation mass transfer proposed by Gibou et al. [3].

The rest of this paper is organized as follows. Section 2 presents the model equations, and their numerical implementation is very briefly referred to in Section 3. In Section 4 we present simulations to verify the correct implementation of the model, and to demonstrate its usefulness in cases of relevance to gas processing. Finally, Section 5 concludes the paper.

2. The mathematical model

In this section we give a brief description of the two-phase flow model. We also discuss how this model was extended to treat heat transport and to account for mass transfer between the phases due to vaporization and condensation.

2.1. The flow model

The mathematical model for the flow is given by the incompressible Navier–Stokes equations. They consist of the incompressibility assumption,

$$\nabla \cdot \boldsymbol{u} = 0, \tag{1}$$

and the momentum-balance equation

$$\rho \left(\frac{\partial \boldsymbol{u}}{\partial t} + (\boldsymbol{u} \cdot \nabla) \boldsymbol{u} \right) = -\nabla p + \nabla \cdot \mu \nabla \boldsymbol{u} + \boldsymbol{f}_{\mathrm{b}} + \boldsymbol{f}_{\mathrm{s}}. \tag{2}$$

Herein, $\boldsymbol{u}$ is the fluid velocity field, ρ is the fluid density, p is the pressure, μ is the viscosity, $\boldsymbol{f}_{\mathrm{b}}$ denotes the body forces and $\boldsymbol{f}_{\mathrm{s}}$ denotes the interfacial forces.

2.2. The heat transport equation

We assume that the fluid has constant density within each phase, the temperature differences in the fluid are small, the fluid velocities are small with respect to the speed of sound, and the viscous heat dissipation is negligible. Under these assumptions the general equation for heat transfer reduces to an advection-diffusion equation for temperature [7, §50],

$$\rho c_p \left(\frac{\partial T}{\partial t} + (\boldsymbol{u} \cdot \nabla) T \right) = \nabla \cdot k \nabla T, \tag{3}$$

where c_p is the specific heat capacity at constant pressure and k is the thermal conductivity.

2.3. The Boussinesq coupling

Time integration of the temperature transport equation (3) alongside the Navier–Stokes equations (1) and (2) gives a temperature field that evolves in time subject to diffusion and advection with the fluid flow. What it does not give is any kind of mechanism through which the temperature can couple to the velocity field and be a driving force of the flow. Physically such a coupling would happen through contraction and expansion of the fluid as it is heated and cooled. In our incompressible flow model, however, we do not allow expansion or contraction. Therefore, if we want to model temperature-driven flows, we have to construct an artificial

coupling. We choose to employ the Boussinesq approximation and introduce a temperature-dependent body force,

$$f_{\mathrm{b}} = \rho g (1 - \beta (T - T_\infty)), \tag{4}$$

where g is the gravitational acceleration vector, β is the thermal expansion coefficient and T_∞ is a reference temperature.

2.4. The level-set method

The level-set method is used to capture and evolve the interface Γ between the two phases. The interface is defined implicitly as the set of points on the zero isocontour of the level-set function ϕ,

$$\Gamma = \{x | \phi(x) = 0\}. \tag{5}$$

We chose the signed distance to the interface to be our level-set function. That is,

$$\phi(x) = \begin{cases} -\min_{y \in \Gamma} (\|x - y\|_2) & \text{if } x \text{ in Phase 1,} \\ +\min_{y \in \Gamma} (\|x - y\|_2) & \text{if } x \text{ in Phase 2.} \end{cases} \tag{6}$$

To make sure that the level-set function continues to represent the signed distance to the interface through the simulation we use the reinitialization procedure by Sussmann et al. [12]. In order to evolve the interface in time, we advect the level-set function ϕ with the interface velocity w using

$$\frac{\partial \phi}{\partial t} + w \cdot \nabla \phi = 0. \tag{7}$$

In the special case when there is no mass vaporization or condensation, the interface velocity is equal to the fluid velocity. In general, however, $w \neq u$. The field of unit vectors n that are normal to the interface is defined in terms of ϕ as

$$n = \frac{\nabla \phi}{\|\nabla \phi\|_2}, \tag{8}$$

and the local curvature of the interface is defined as

$$\kappa = -\nabla \cdot n. \tag{9}$$

2.5. The phase-transition model

The motivation for introducing a phase-transition model is that we wish to model situations where we have two phases, liquid and gas, of the same substance and there is mass transport between the two phases, i.e. vaporization or condensation. The model described here is identical to that proposed by Gibou et al. [3].

The general idea is to impose the constraint that the interface temperature must be equal to the saturation temperature of the liquid, T_{sat}. This may lead to an interfacial jump in the normal component of the conductive heat flux $q = -k \nabla T$, which is then used to find a mass flux across the interface that is consistent with the jump. Specifically, when more heat flows into a point on the interface than flows out, we assume that this heat has been absorbed in the vaporization of some of the liquid around that point, and vice versa when more heat flows out than in.

From these assumptions, we can calculate the component of the mass flux m normal to the interface as

$$m = \frac{[-n \cdot k \nabla T]}{\Delta h}, \tag{10}$$

where Δh is the specific enthalpy difference associated with the phase transition from Phase 2 to Phase 1. The brackets denote the interfacial jump in the bracketed quantity, that is the difference between the value of the bracketed quantity in Phase 2 and its value in Phase 1.

From mass conservation at the interface, we get an expression for the interface velocity w in terms of the Phase 1 velocities u^-,

$$w = u^- - \frac{m}{\rho^-} n. \tag{11}$$

Note that interface velocity w reduces to the fluid velocity u when $m = 0$, i.e. when there is no vaporization or condensation.

2.6. The jump conditions

In order to treat the interfacial discontinuities sharply, we must be able to compute the jumps in some properties that are discontinuous at the interface.

For regular, two-phase flow the velocity is continuous, so its jump condition is

$$[u] = 0. \tag{12}$$

In contrast, the pressure may be discontinuous and has a jump [5]

$$[p] = 2[\mu] n \cdot \nabla u \cdot n + \sigma\kappa, \tag{13}$$

where κ is the local interface curvature and σ is the coefficient of interfacial tension. If the two phases have different viscosities, we may also have a discontinuous viscous stress [5],

$$[\mu\nabla u] = [\mu]\{(n \cdot \nabla u \cdot n) nn + (n \cdot \nabla u \cdot t) nt - (t \cdot \nabla u \cdot n) tn + (t \cdot \nabla u \cdot t) tt\}, \tag{14}$$

where t is a unit vector tangential to the interface.

When modelling two-phase flow while accounting for phase transitions, the velocity may no longer be continuous at the interface. It is discontinuous if we have a non-zero mass flux m and different densities in the two phases. Applying mass conservation at the interface, we get an expression for the jump in the fluid velocity,

$$[u] = m \left[\frac{1}{\rho}\right] n. \tag{15}$$

Also, the pressure jump now becomes

$$[p] = [\mu n \cdot \nabla u \cdot n] + \sigma\kappa - m^2 \left[\frac{1}{\rho}\right]. \tag{16}$$

The differences in this equation compared to (13) can be attributed to the fact that u is no longer continuous at the interface and that mass is accelerated across the interface when m and the difference in densities is non-zero. As commented by Gibou et al. [3], it is not clear how to treat the viscous stress sharply when simulating phase transitions, so we do not give an expression for $[\mu\nabla u]$ and do not treat the viscous stress sharply in these cases.

3. Implementation

The model equations are integrated in time using strong stability-preserving (SSP) Runge–Kutta (RK) methods and Chorin's projection method. The projection method yields a Poisson equation for the pressure [5] which is solved by the biconjugate gradient stabilized (BCGS) method. All spatial derivative operators are discretized using a central difference (CD) scheme, except for the advective operators where the weighted essentially non-oscillatory (WENO) scheme [9] is used. The GFM is employed to treat the interfacial discontinuities in all terms, except for the viscous stress in cases with phase transitions. In these cases the CSF method is used. As the errors in both the GFM and in the CSF method are first-order in the linear grid size, we cannot expect the overall convergence rate to be better than first-order. For a more detailed discussion of the numerical schemes, the reader is referred to Gibou et al. [3], Gjennestad [4], Ervik et al. [2].
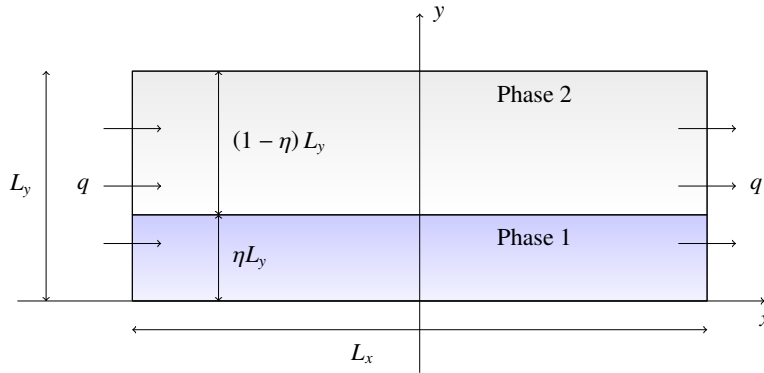
Figure 1: Schematic illustration of the configuration in the two-layer convection case.

4. Simulations

In this section, we present three examples of simulations of heat transport and mass transfer between phases that the heat transport and phase transition models allow us to do. The two first examples are rather simple ones. These cases, and the physical parameters used, are chosen to verify that the implemented methods are able to solve the model equations. The third example will illustrate the model's capability to deal with a more physically realistic problem.

4.1. Two-layer convection

This case is an example of temperature-driven two-phase flow, without any phase transition. A two-dimensional, rectangular cavity of length L_x, height L_y and aspect ratio $A = L_x/L_y$ contains two phases, Phase 2 on top of Phase 1 in a two-layer configuration. A constant and uniform heat flux of magnitude q points into the domain on the western wall and a heat flux of the same magnitude points out of the domain on the eastern wall, as illustrated in Figure 1. The northern and southern walls are thermally insulating.

The size of the domain used in the numerical simulation was $L_x = 0.8\,\text{m}$ and $L_y = 0.1\,\text{m}$, with the interface located at the constant-y line defined by $y = \eta L_y = 0.05\,\text{m}$. The initial temperature was set to 290 K in the entire inner domain and the gravitational acceleration vector $\boldsymbol{g}_\infty$ was set to $-9.81\,\text{m} \cdot \text{s}^{-2}$ along the y-axis. The heat flux q used was $1.0\,\text{W} \cdot \text{m}^{-2}$. The relevant fluid properties are given in Table 1.

This case was run to $t = 10^3\,\text{s}$ and compared to the analytical solution given by Wang et al. [14]. A derivation of the equations needed to verify this solution is presented in [4]. The analytical solution for this case is, strictly speaking, valid only when $A \to \infty$. However, Oueslati et al. [11] claimed that using $A = 8$, as we do, was sufficient to accurately simulate the situation considered in the steady-state analytical solution.

The resulting horizontal velocity component along the vertical centre line of the cavity is shown in Figure 2 for a selection of grid sizes. We observe a buoyancy-driven convection cell in the top layer (Phase 2) where the fluid moves clockwise, and we see a viscosity-driven cell in the bottom (Phase 1), where the

Table 1: Fluid parameters used in the numerical simulation of the two-layer convection case.

	Unit	Phase 1	Phase 2
ρ	$\text{kg} \cdot \text{m}^{-3}$	1.5	1.0
μ	$\text{Pa} \cdot \text{s}$	$2.0 \cdot 10^{-5}$	$1.0 \cdot 10^{-5}$
c_p	$\text{J} \cdot \text{kg}^{-1} \cdot \text{K}^{-1}$	$1.2 \cdot 10^2$	$1.0 \cdot 10^2$
κ	$\text{W} \cdot \text{K}^{-1} \cdot \text{m}^{-1}$	$1.3 \cdot 10^{-2}$	$1.0 \cdot 10^{-2}$
β	K^{-1}	$1.0 \cdot 10^{-4}$	$1.0 \cdot 10^{-3}$
T_∞	K	$2.9 \cdot 10^2$	$2.9 \cdot 10^2$

Table 2: Convergence rate, n, for the two-layer convection case. N_y is the number of grid cells in the y-direction.

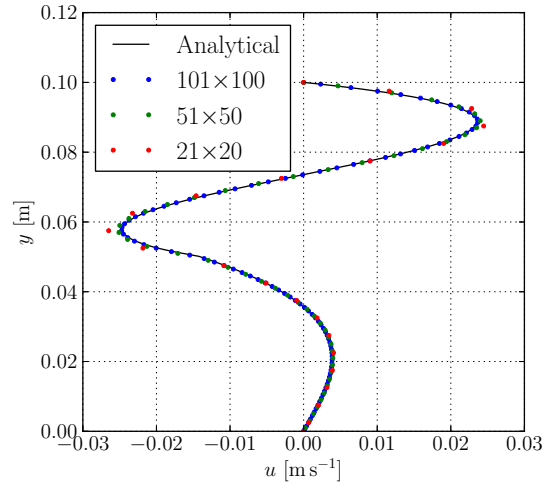| N_y	u_{max}	E_{abs}	n
-	$\text{m} \cdot \text{s}^{-1}$	$\text{m} \cdot \text{s}^{-1}$	-
21	$2.483 \cdot 10^{-2}$	$1.30 \cdot 10^{-3}$	-
31	$2.438 \cdot 10^{-2}$	$8.54 \cdot 10^{-4}$	1.08
51	$2.400 \cdot 10^{-2}$	$4.72 \cdot 10^{-4}$	1.19
81	$2.382 \cdot 10^{-2}$	$2.89 \cdot 10^{-4}$	1.05
101	$2.367 \cdot 10^{-2}$	$1.38 \cdot 10^{-4}$	3.36

Figure 2: Comparison of selected numerically obtained velocity profiles along the vertical centre line in the two-layer convection case with the analytical solution. It is evident that the numerical solutions approach the analytical solution upon grid refinement.

Table 3: Fluid parameters used in the growing vapour-film case

	Unit	Phase 1	Phase 2
ρ	$kg \cdot m^{-3}$	1.0	$2.0 \cdot 10^{-1}$
μ	$Pa \cdot s$	$1.0 \cdot 10^{-5}$	$1.0 \cdot 10^{-5}$
c_p	$J \cdot kg^{-1} \cdot K^{-1}$	1.0	5.0
k	$W \cdot K^{-1} \cdot m^{-1}$	1.0	1.0

Table 4: Convergence order, n, for the growing vapour-film case. N_x is the number of grid cells in the x-direction.

N_x	$\eta(0.6\,s)$	E_{abs}	n
-	m	m	-
11	$7.799 \cdot 10^{-1}$	$5.34 \cdot 10^{-3}$	-
21	$7.773 \cdot 10^{-1}$	$2.74 \cdot 10^{-3}$	1.03
41	$7.760 \cdot 10^{-1}$	$1.44 \cdot 10^{-3}$	0.97
81	$7.753 \cdot 10^{-1}$	$7.28 \cdot 10^{-4}$	1.00

fluid moves anti-clockwise. To plotting accuracy, there is good agreement between the analytical solution and the numerical results for the 101×100 grid. Furthermore, the numerical solutions appear to approach the analytical solution when the grid is refined.

To do a quantitative comparison between the analytical solution and the numerical results, we consider the maximum of the horizontal velocity component u_{max} along the vertical centre line. We locate the u_{max} from the numerical results by doing a fourth-order polynomial interpolation around the maximum and finding the maximum of the polynomial. In the analytical solution, u_{max} was found to be $2.3557 \cdot 10^{-2}\,m \cdot s^{-1}$. A convergence table based on the absolute error E_{abs} in u_{max} for different grid sizes, with the analytical value as reference, is shown in Table 2. According to the estimated orders of convergence n from this table, the convergence to the analytical solution upon grid refinement is of first-order.

We can conclude that there is agreement between the numerical results and the analytical solution. Also, we have demonstrated the expected first-order convergence rate of our method when refining the grid.

4.2. A growing vapour film

The first case we consider with phase transition is a one-dimensional growing vapour film. It is interesting because it has analytical solutions for the temperature and velocity fields and for the interface location. Also, it was simulated by Gibou et al. [3]. Thus this case provides a reference solution to which the results from our simulations can be compared. The analytical solution and a derivation of the expressions needed to verify it can be found in Gjennestad [4].

We have a fluid domain of length $L = 1.0\,m$, occupied by a liquid (Phase 1) and a gaseous phase (Phase 2) of the same substance. The two phases are separated by an interface located at $x = \eta(t)$, as shown in
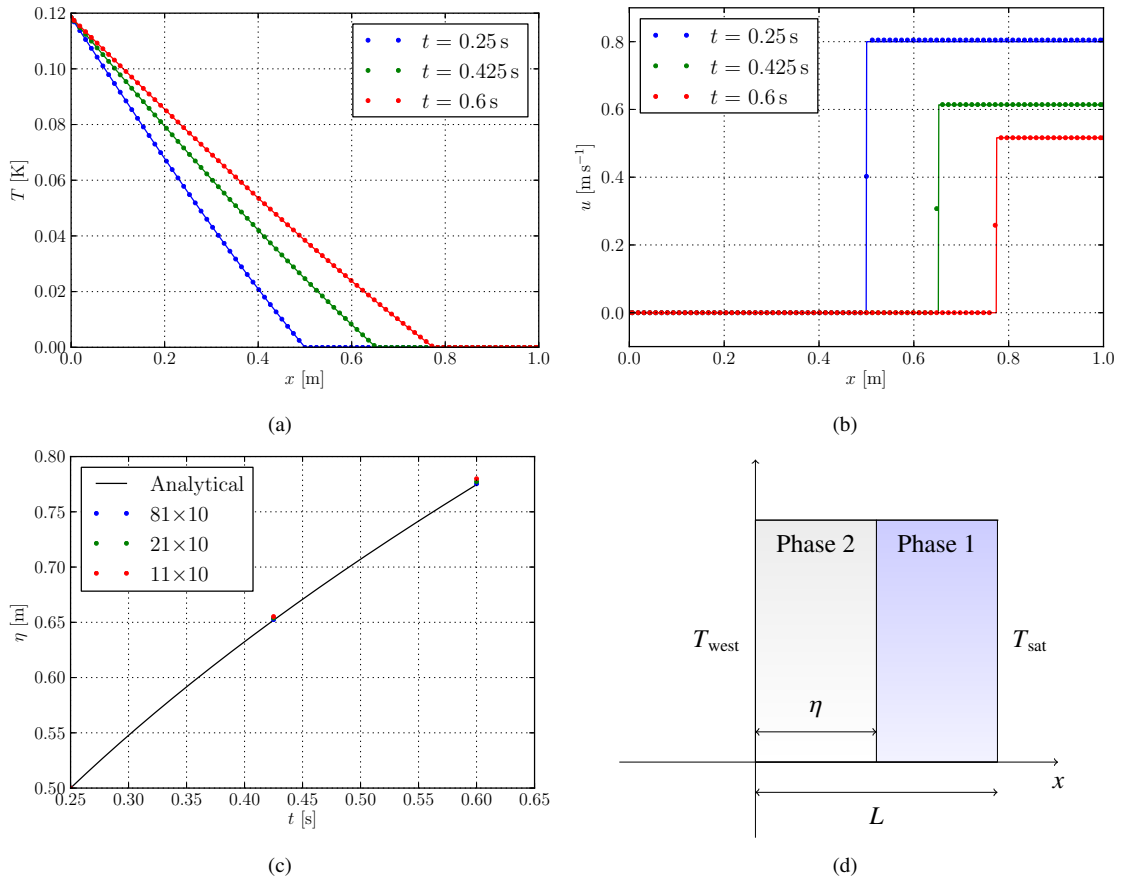
Figure 3: The growing vapour-film case. (a) The temperature profiles obtained on the 81×10 grid at different times. The analytical solution at each time is drawn as a solid line. (b) The velocity profiles obtained on the 81×10 grid at different times. The analytical solution at each time is drawn as a solid line. (c) A plot of the interface location η against time t obtained on a selection of grid sizes. The analytical solution is shown as a solid line. (d) Schematic drawing of the initial fluid configuration. Phase 1 is the liquid and Phase 2 is the gaseous phase. The eastern wall is held at the saturation temperature T_{sat} and the western wall is held at $T_{\text{west}} > T_{\text{sat}}$.

Figure 3d. The specific enthalpy difference associated with the phase transition is $\Delta h = -1.0 \cdot 10^{-3} \, \text{J} \cdot \text{kg}^{-1}$. The other relevant fluid parameters are given in Table 3. Although the case is one-dimensional, it was simulated in a two-dimensional domain. The obtained solution was then invariant upon translation normal to to the x-axis.

The northern, southern and western walls have free-slip boundary conditions (BCs) and the eastern wall has an outflow condition. We impose homogeneous Neumann (zero-gradient) BCs on the pressure at all walls except the eastern wall, where we demand $p = 0 \, \text{Pa}$. Further, we hold the temperature on the western wall constant, $T_{\text{west}} = 0.1185 \, \text{K}$, and the temperature on the eastern wall constant and equal to the saturation temperature, $T_{\text{sat}} = 0 \, \text{K}$. By imposing homogeneous Neumann BCs on the temperature at the northern and southern walls, these are thermally insulating.

The initial time is $t = 0.25 \, \text{s}$ and the initial interface location is $\eta(0.25 \, \text{s}) = 0.5 \, \text{m}$. Both the temperature and the velocity profiles were initialized according to the analytical solution. The simulations were run from $t = 0.25 \, \text{s}$ to $t = 0.6 \, \text{s}$ on five different grid sizes, 11×10, 21×10, 41×10 and 81×10.

The obtained temperature profiles on the 81×10 grid are shown in Figure 3a at the initial time $t = 0.25 \, \text{s}$, the final time $t = 0.6 \, \text{s}$ and at $t = 0.425 \, \text{s}$. At each time the analytical solution is also shown as a solid line. From inspecting Figure 3a, we see that the jump in $\partial T / \partial x$ at the interface decreases with time. Therefore, we expect the jump in velocity to decrease too, in accordance with (10) and (15). We can also conclude that

there is agreement between the simulation results and the analytical solution to plotting accuracy.

The velocity profiles obtained on the same 81×10 grid at the same points in time are shown in Figure 3b. Again the analytical solution at each point in time is shown for comparison. From inspecting this figure, we see that the velocity jump at the interface does indeed decrease with time, as expected from the temperature profiles in Figure 3a. Overall, we conclude that there is good agreement between the simulated and analytical velocity profiles to plotting accuracy.

The interface location η obtained from simulations on a selection of grid sizes is plotted against time t in Figure 3c. The corresponding analytical solution is also shown for comparison. It is evident that $\eta(t)$ is somewhat overestimated, especially on the coarse 11×10 and 21×10 grids. However, it is also evident that the simulation results approached the analytical solution upon grid refinement and that there is agreement, to plotting accuracy, between the simulated results on the 81×10 grid and the analytical solution.

To quantify the extent of the agreement between the simulated and the analytical results, a convergence study based on the absolute error E_{abs} in $\eta(0.6\,\text{s})$ with respect to the analytical solution, $0.7746\,\text{m}$, was performed. The results are given in Table 4. These results, in particular the estimated orders of convergence, n, are consistent with the first-order convergence rate we would expect from the first-order GFM treatment of the interface conditions.

We can conclude that there is agreement between the numerical results and the analytical solution to the temperature and velocity profiles and the interface location. Also, we have demonstrated the expected first-order convergence rate of our method for solving the model when phase transitions are accounted for.

4.3. A vaporizing methane droplet

In this case we consider a vaporizing droplet of methane in 3D. The simulations were performed on a two-dimensional 100×200 grid under the assumption of rotational symmetry around the y-axis.

Initially, we have a spherical droplet of liquid methane (Phase 1) of radius $2.0 \cdot 10^{-3}\,\text{m}$ located at the centre of the domain. It is surrounded by a phase of gaseous methane (Phase 2). The fluids are initialized to be at rest and to have a uniform temperature equal to the saturation temperature $T_{\text{sat}} = 111.51\,\text{K}$. This saturation temperature corresponds to an equilibrium pressure of 1 bar.

The surface tension coefficient between the two phases is $\sigma = 1.3335 \cdot 10^{-2}\,\text{N} \cdot \text{m}^{-1}$ and there is no gravity. The specific enthalpy difference associated with the phase transition is $\Delta h = -5.1112 \cdot 10^{5}\,\text{J} \cdot \text{kg}^{-1}$. Table 5 contains the rest of the relevant fluid parameters. The methane fluid data were extracted from [8].

To have a supply of thermal energy to drive the vaporization, we set Dirichlet BCs on the temperature $T = 300.0\,\text{K}$ and inflow BCs on the velocity at the top and bottom. The inflow velocities are ramped up linearly to $5.0 \cdot 10^{-3}\,\text{m} \cdot \text{s}^{-1}$ in $0.2\,\text{s}$.

We wish to allow the gas flowing in and the gas from the vaporizing drop to escape freely, so the radial boundary carries an outflow condition for the velocity and a zero-gradient condition for the temperature. Homogeneous Neumann BCs were imposed for the pressure at the top and bottom boundaries. At the radial boundary we set $p = 0\,\text{Pa}$.

Figure 4a shows the droplet interfaces at $t = 0.0\,\text{s}$ and at $t = 3.0\,\text{s}$. As we might have expected, the droplet has shrunk due to the vaporization. It has also kept its spherical shape.

In Figure 4b the droplet interface and an illustration of the velocity field at $t = 3.0\,\text{s}$ are shown. Looking at the velocity field, we see that gas flows into the domain at the top and bottom boundaries, mixes with the vaporized gas from the droplet and is allowed to flow out across the side boundary.

Table 5: Fluid parameters used in the vaporizing methane droplet case

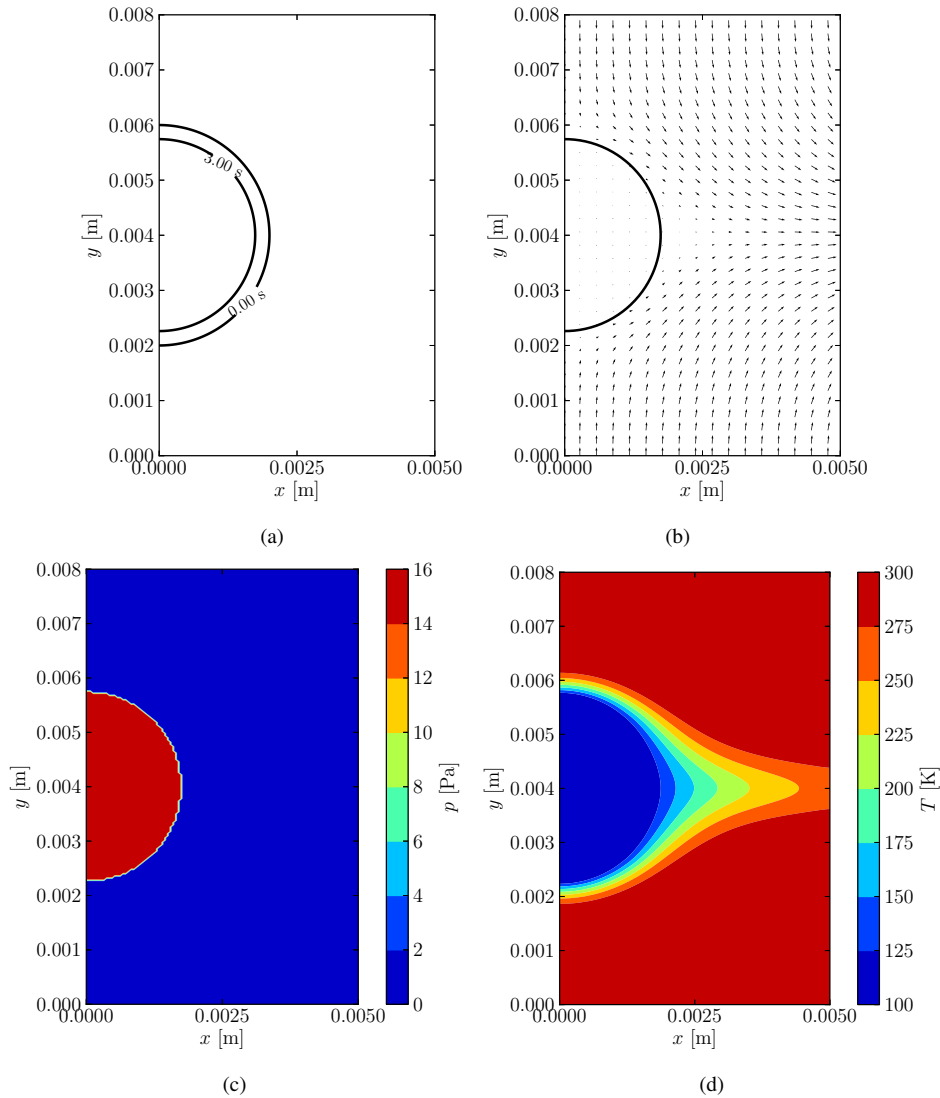|	Unit	Phase 1	Phase 2
ρ	$\text{kg} \cdot \text{m}^{-3}$	$4.2259 \cdot 10^{2}$	1.7946
μ	$\text{Pa} \cdot \text{s}$	$1.1720 \cdot 10^{-4}$	$4.4579 \cdot 10^{-6}$
c_p	$\text{J} \cdot \text{kg}^{-1} \cdot \text{K}^{-1}$	$3.4799 \cdot 10^{3}$	$2.2165 \cdot 10^{3}$
k	$\text{W} \cdot \text{K}^{-1} \cdot \text{m}^{-1}$	$1.8409 \cdot 10^{-1}$	$1.1561 \cdot 10^{-2}$

Figure 4: Plots from the vaporizing methane droplet case showing (a) the interface locations at $t = 0.0$ s and at $t = 3.0$ s, (b) the interface at $t = 3.0$ s with an illustration of the velocity field, (c) the pressure field at $t = 3.0$ s and (d) the temperature field at $t = 3.0$ s.

The pressure field at $t = 3.0$ s is shown in Figure 4c. Because there is no gravity, the pressure is almost uniform within each phase. At the surface there is a pressure jump, as we would expect from the jump condition (16). In this case $\kappa\sigma \approx 17$ Pa, so the contribution from the surface tension forces is the most important.

Figure 4d shows the temperature field at $t = 3.0$ s. Heat is advected with the fluid flow from the top and bottom boundaries and towards the middle of the domain and the droplet, where it drives the vaporization. The isotemperature curves are denser near the top and bottom of the droplet, and thus heating is larger here. From the uneven heating of the droplet and from (10), we know that there is a larger vaporization mass flux at the top and bottom compared to the sides. Due to the unevenly distributed vaporization mass flux at the surface, we might expect that the droplet should lose its spherical shape. However, by looking back to Figure 4a, we see that this is not the case. Evidently, the surface tension forces are large enough to cause internal flow in the droplet to compensate for the larger amount of mass lost due to vaporization at the top and bottom.

These results show that the model can be used to simulate a case with physically realistic fluid parameters and yield results in agreement with what we would qualitatively expect.

5. Conclusions

We have described models for heat transport and mass transfer between phases due to vaporization and condensation. They have been implemented in a framework for detailed two-phase flow calculations based on the level-set method.

For two test cases, we have shown that simulated results agree with the corresponding analytical solutions and we have demonstrated first-order convergence of the implemented methods. Thus we have verified that the implemented methods correctly solve the model equations for these cases.

We have also simulated a physically realistic, three-dimensional case that is assumed rotationally symmetric around an axis. In this case a droplet of liquid methane was vaporized and it was shown that the model yielded results that were consistent with qualitative expectations. The successful simulation of this case shows that the implemented methods are able to handle the simulation of a case involving phase transition in natural gas.

Through further and detailed numerical studies, it is hoped that the implemented models described herein will aid in obtaining a better and more detailed understanding of relevant experimental results and of the underlying physical behaviour of the fluid streams involved in natural gas liquefaction. This in turn may ultimately lead to a more energy-efficient liquefaction process.

Acknowledgements

References

[1] Dhir, V. K., 2001. Numerical simulations of pool-boiling heat transfer. AIChE Journal 47 (4), 813–834.

[2] Ervik, Å., Lervåg, K. Y., Munkejord, S. T., Jan. 2014. A robust method for calculating interface curvature and normal vectors using an extracted local level set. Journal of Computational Physics 257, 259–277.

[3] Gibou, F., Chen, L., Nguyen, D., Banerjee, S., 2007. A level set based sharp interface method for the multiphase incompressible Navier–Stokes equations with phase change. Journal of Computational Physics 222, 536–555.

[4] Gjennestad, M. Aa., June 2013. Modeling heat transfer in two-phase flow using the level-set method. Master's thesis, Department of Physics, Norwegian University of Science and Technology.

[5] Kang, M., Fedkiw, R., Liu, X., 2000. A boundary condition capturing method for multiphase incompressible flow. Journal of Scientific Computing 15, 323–360.

[6] Kunugi, T., 2012. Brief review of latest direct numerical simulation on pool and film boiling. Nuclear Engineering and Technology 44 (8), 847–854.

[7] Landau, L. D., Lifshitz, E. M., 1987. Fluid Mechanics, 2nd Edition. Vol. 6 of Course of Theoretical Physics. Butterworth–Heinemann.

[8] Linstrom, P., Mallard, W. (Eds.), 2014. NIST Chemistry WebBook, NIST Standard Reference Database Number 69. National Institute of Standards and Technology, Gaithersburg MD, 20899.

[9] Osher, S., Fedkiw, R., 2003. Level Set Methods and Dynamic Implicit Surfaces. Springer.

[10] Osher, S., Sethian, J. A., 1988. Fronts propagating with curvature-dependent speed: Algorithms based on Hamilton–Jacobi formulations. Journal of Computational Physics 79, 12–49.

[11] Oueslati, F. S., Bennacer, R., Sammouda, H., Ganaoui, M. E., 2012. Analytical and numerical solutions for natural convection in a shallow cavity filled with two immiscible fluids: Shear stress action. Numerical Heat Transfer; Part A: Applications 62 (8), 605–623.

[12] Sussmann, M., Smereka, P., Osher, S., 1994. A level set approach for computing solutions to incompressible two-phase flow. Journal of Computational Physics 114, 149–159.

[13] Tamura, I., Tanaka, T., Kagajo, T., Kuwabara, S., Yoshioka, T., Nagata, T., Kurahashi, K., Ishitani, H., 2001. Life cycle CO_2 analysis of LNG and city gas. Applied Energy 68 (3), 301–319.

[14] Wang, C. H., Sen, M., Vasseur, P., 1991. Analytical investigation of Bénard–Marangoni convection heat transfer in a shallow cavity filled with two immiscible fluids. Applied Scientific Research 48 (1), 35–53.